

## Inherent Thermal-Noise Problem in Addressing Qubits

Slawomir Simbierowicz<sup>1</sup>,<sup>†</sup> Massimo Borrelli<sup>2</sup>, Volodymyr Monarkha<sup>2</sup>, Ville Nuutinen, and Russell E. Lake<sup>1\*</sup>

*Bluefors Oy, Arinatie 10, Helsinki 00370, Finland*

 (Received 4 January 2024; revised 28 March 2024; accepted 28 May 2024; published 2 July 2024)

Qubit-specific measurement in a superconducting quantum processor requires physical interconnects that traverse 4 orders of magnitude in temperature from 293 K to 10 mK. Although the quantum processor can be thermalized and shielded from electromagnetic noise, the interconnects themselves introduce an unavoidable remote heat bath that causes decoherence of quantum states. In the present work, we report quantitative and device-independent measurements of the power radiated to the quantum processor from its control lines. Our results have been obtained using a calibrated bolometer that operates within a millikelvin environment with time-resolved measurement capability. In the limit of zero applied power, the noise power emitted to the quantum processor is equivalent to that of a blackbody with temperature 63–71 mK for the prototypical drive lines in the study. Experimentally, we increase the applied power of a simulated control signal to map out the resulting temperature rise and thermal time constant of five prototypical drive-line varieties. We input the data to an open quantum system model to demonstrate the trade-off between dissipated signal power, transmon-qubit lifetime, pure dephasing, gate fidelity, and the implied decoherence rates due to self-heating during microwave operations. Beyond explaining dephasing rates observed in the literature, our work sets the stage for accurate noise modeling in novel quantum computer interfacing methods due to our device-agnostic approach.

DOI: [10.1103/PRXQuantum.5.030302](https://doi.org/10.1103/PRXQuantum.5.030302)

### I. INTRODUCTION

Continuous operation of a quantum computer contained within a dilution refrigerator requires proper cooling of its individual building blocks, including coaxial cabling, microwave attenuators, filters, amplifiers, and the superconducting quantum chip at millikelvin temperatures [1,2], often operating in the circuit quantum electrodynamics band of 5–15 GHz [3]. To facilitate microwave control by coupling to the qubit or dispersive readout through a resonator mediating interaction with the qubit, interconnects such as coaxial lines are needed between room-temperature electronics and the chip at the coldest stage and, unavoidably, these carry broadband thermal noise that locally heats up the circuit element to which it is coupled. At elevated temperatures of the resonator, the coherence of the quantum state of the qubit is subjected to deleterious pure dephasing [4,5], which lowers the coherence

time  $T_2^*$  of the qubit below its theoretical bound of 2 times the energy relaxation time  $T_1$ —which, in turn, has some sensitivity to heat coupled to the qubit itself [6,7]. As a remedy, the input lines are attenuated in stages all the way down to the millikelvin stage both for gradual dissipation of microwave signals in individual components and reduction of noise emitted into the device [2]. Conversely, the weak readout signals return on low-loss output lines and are amplified with quantum limited amplifiers and postamplifiers that cause unwanted back-action noise [6] on the qubit, mitigated with microwave isolators and filters [8]. Despite all the counter-measures, typical  $T_2^*$  times fall short of the relaxation-limited upper bound [9–16], calling for further improvements in signal conditioning [17,18], while qubit lifetimes already begin to reach the 1-ms barrier [13,19–21].

To understand the connection between dephasing times and the temperature of the photonic bath of the drive line, it is instructive to consider the residual photon number in the readout resonator of the qubit. The photon-shot noise in the drive line at angular frequency  $\omega$  and equivalent blackbody temperature  $T_{\text{bb}}$  follows the Bose-Einstein statistics [2]:

$$n_{\text{BE}}(T_{\text{bb}}, \omega) = \left[ \exp\left(\frac{\hbar\omega}{k_{\text{B}}T_{\text{bb}}}\right) - 1 \right]^{-1}, \quad (1)$$

\*Contact author: [russell.lake@bluefors.com](mailto:russell.lake@bluefors.com)

†Contact author: [slawomir.simbierowicz@bluefors.com](mailto:slawomir.simbierowicz@bluefors.com)

*Published by the American Physical Society under the terms of the [Creative Commons Attribution 4.0 International](https://creativecommons.org/licenses/by/4.0/) license. Further distribution of this work must maintain attribution to the author(s) and the published article's title, journal citation, and DOI.*

where  $k_B$  is the Boltzmann constant and  $\hbar$  is the reduced Planck constant. For example, at a typical resonator frequency of 6 GHz, the difference between an attenuator emitting noise at 30 mK and 40 mK translates to a tenfold increase in the photon number from  $7 \times 10^{-5}$  to  $7 \times 10^{-4}$ . If we then assume that the readout resonator thermalizes with the photon bath of the drive line and recall that the pure dephasing rate is directly proportional to the photon number in the readout resonator [22–24], we find that it is similarly increased tenfold. Yet, such low temperatures are difficult to achieve in practice, with typical drive-line temperatures falling between 35 and 140 mK [11–13,17,18,25–30], where large differences are only partially explained by different drive-line configurations.

As a key limiting factor, the attenuators in the drive line are most often constructed from a network of thin-film resistors with a volume-dependent heat capacity  $C$ , where electrons stay hot due to a poor coupling with the phonon bath [17,31]. The weak electron-phonon coupling is often a bottleneck for thermal conductance  $G$ , leading to latency times  $\tau = C/G$ . This has not been extensively characterized for drive lines yet, while recognizing a recent effort in Ref. [30] that used a transmonlike thermal detector to capture slow latencies between tens of minutes and up to hours. We speculate that faster noise processes set the physical maximum depth for any quantum algorithm implemented with microwave gate pulses applied through the drive line. Self-heating in the attenuators would eventually result in optimized gate fidelities dropping below 99%, which is currently understood as uncorrectable with surface codes [32]. Crucially, attenuator overheating is a threat to the present race to scale up quantum computers with denser wiring technologies [33–35] increasing the temptation for excessive miniaturization of thin-film electron volumes, even though cryogenic signal generation technologies [36] and alternative wiring solutions such as photonic links are on the horizon [37,38].

Presently, there is a distinct lack of systematic experimental studies in both drive-line thermodynamics and standardized methodology to access elementary system parameters. In contrast to previous quantum thermodynamics experiments in mesoscale systems [39–41], we study relatively large objects: the microwave attenuator in the drive line, in particular. Furthermore, we do this in a noninvasive fashion by detecting the emitted blackbody radiation in the coaxial line, using a time-resolving power detector. While there exists a handful of other cryogenic power sensors that appear promising for this type of measurement [30,42], we employ a coaxially coupled ultrasensitive nanobolometer, previously introduced in Refs. [43–46]. The reported noise-equivalent powers below  $60 \text{ zW}/\sqrt{\text{Hz}}$  and detector response times reaching  $20 \text{ }\mu\text{s}$  demonstrate the potential for our experiments.

A critical and difficult part of cryogenic power sensing is calibration at the reference plane of the quantum

device. In Ref. [45], the detector was traceable to the Systeme International (SI) voltage standard owing to calibration through dc substitution: measuring the dissipated dc power in on-chip resistors and equating the detector response to an equivalent ac power drive resulted in accurate estimates of the line attenuation in a wide frequency band between 50 MHz and 7 GHz. Here, we do not include on-chip dc heaters and instead demonstrate a detector-independent calibration method using a known external rf power source, which we realize with a coaxially coupled cryogenic blackbody radiation source that we have previously introduced in Ref. [47]. In brief, the wide-band variable-temperature  $50\text{-}\Omega$  noise source is equipped with a heater and a ruthenium oxide thermometer calibrated against a magnetic field fluctuation thermometer with traceability to primary standards [48,49]. In previous work, such a noise source has been employed as a hot-cold load [50] cascaded with cryogenic amplifiers and a spectrum analyzer at room temperature; by studying the amplified noise, the noise temperature of the cascade could be determined. Here, we use this method in reverse by investigating the attenuated noise using our *in situ* detector as the spectrum analyzer, with the end goal of revealing residual excess noise from overheated electrons. This present work studies the qubit-thermalization problem in the context of blackbody radiation injected through the drive line but, more broadly, the problem applies to other noise baths, including nonequilibrium quasiparticles [51,52], that in turn could be generated by ionizing [53] or infrared radiation that is nonthermal [54]. The hierarchy of importance for each of these mechanisms depends on the quantum processor implementation [55]. However, in contrast to the other dephasing mechanisms, the experimentalist has a greater degree of control over drive-line thermalization than the other decoherence effects by selection of the signal-conditioning methods [2].

This paper is organized as follows. First in Sec. II, we develop new methodology for calibrating microwave powers around a femtowatt using the blackbody noise source. Using the same calibration, we heat up the drive line with a microwave tone in the rejection band of the detection circuit and observe the noise temperature dependence against the applied power. Switching to a lock-in measurement, we pulse the detuned rf drive revealing thermal latencies. Second in Sec. III, we apply our method systematically around 6 GHz to five typical qubit drive lines and retrieve the attenuation coefficients, noise temperatures with either zero or varying rf drive, and the thermodynamical quantities  $\tau$ ,  $C$ , and  $G$ . Third in Sec. IV, we interpret our results using an open quantum system approach, converting the obtained temperatures to corresponding  $T_1$  and  $T_2^*$  times for typical qubit parameters, and we estimate the fidelity of some single- and two-qubit operations. Finally, we summarize our conclusions in Sec. V.

## II. EXPERIMENTAL METHODS

The power detector is a nanobolometer that can detect the radiated microwave power from a coaxially coupled signal source at millikelvin temperatures. In Fig. 1, we display a schematic of the detection-and-calibration configuration along with the observed response of the detector. In Secs. II A and II B, we will first discuss the detector, its calibration, and operation for sensing of constant microwave drive either single-frequency tones or wide-band noise. Second, we will discuss the time-resolving mode to the application of pulsed microwave signals and explain how we extend our calibration to such measurements captured in Fig. 2.

### A. Detector in steady-state operation

#### 1. Operating principle

The bolometer in Fig. 1(a), illustrated inside the dashed area and shown in the optical micrograph, is a thermal detector that has been lithographically fabricated on a silicon microchip and installed at the millikelvin temperature

stage of a cryogenic system. We couple coaxially to its two distinct ports for microwave signals: (1) a “heater input” port for the unknown incoming microwave signals to be absorbed and analyzed by the bolometer and (2) a resonant circuit “probe” port where we readout the corresponding response of the detector in an rf reflection measurement. The two ports are thermally coupled through a gold-palladium nanowire but are electrically decoupled by capacitors  $C_1$ ,  $C_2$ , and  $C_g$ . The high sensitivity and low noise-equivalent power (NEP) of the bolometer stem from the fact that the absorber is comprised of a nanowire element that minimizes the thermal conductance to the environment. The input port (1) of the bolometer terminates on chip in a nominally impedance-matched resistive section of the normal-metal nanowire to absorb incoming microwave heater power. The absorbed microwave power increases the electron temperature throughout the nanowire and manifests itself as an increase in the Josephson inductance in the series of superconducting–normal-metal–superconducting (SNS) junctions on the “probe” section of the nanowire indicated as “X” in Fig. 1(a). The resonant circuit coupled to port (2) is defined by the SNS

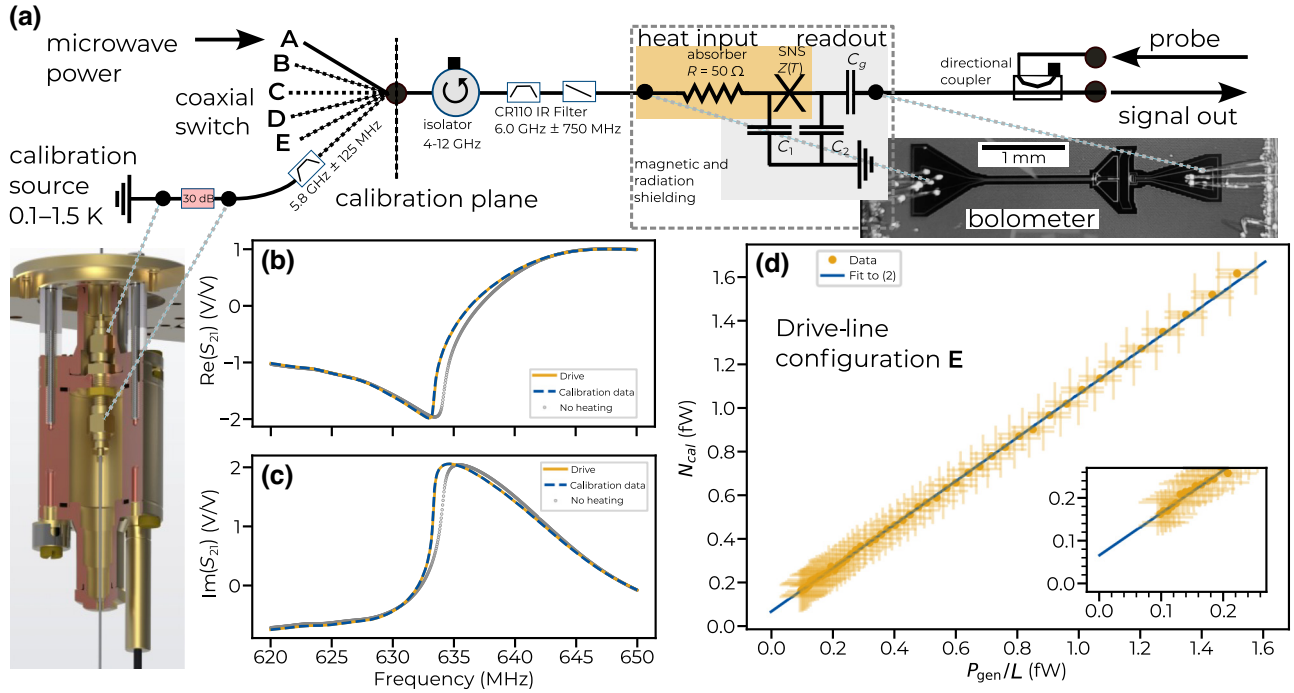


FIG. 1. The detection principle and calibration. (a) The detector is shown in the optical micrograph and depicted schematically inside the dashed area: on the heater port (orange), heat is absorbed to the 50-Ω nanowire, altering the SNS inductance and therefore the resonance frequency of the readout tank circuit (gray). Readout is performed in reflection with the aid of a directional coupler. On the heater side, coaxial switches toggle between drive lines A–E and a calibration source: a variable-temperature blackbody source. Band-pass filtering is utilized to select a suitable noise bandwidth and an isolator mitigates detector back action. (b),(c) The real and imaginary parts of the resonance line shape, normalized with the blue-detuned magnitude and phase. The gray traces correspond to zero applied heater power, whereas yellow and blue correspond to a drive-line input and the closest calibration power, respectively. (d) Fitting calibrated rf powers to a set of generator powers yields the attenuation factor (slope) and effective drive-line temperature (offset). Here, the horizontal axis is normalized with the attenuation. The inset shows an enlargement at low powers, revealing nonzero vertical offset.

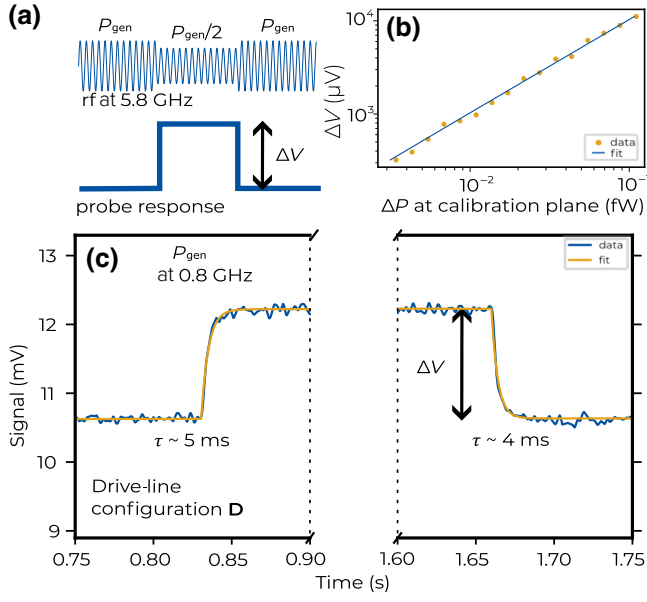


FIG. 2. The time-domain analysis of the drive lines. (a) Readout is performed at a single probe frequency using a lock-in amplifier. The rf drive at 5.8 GHz is modulated with a 3-dB step reduction in power for 830 ms every 8 s. This corresponds to a sharp increase in the readout signal. (b) A calibration curve is obtained as a straight-line fit to repeated experiments at different powers. (c) Use of the same modulation pattern at 0.8 GHz with several orders of magnitude higher power leads to a delayed thermal response of the drive line.

junction in parallel with the on-chip capacitors, which has a resonance frequency around 600 MHz that is sensitive to the electron temperature, thus making the device a viable detector via reflectometry.

## 2. Calibration

Incoming signals are coaxially coupled to the detector input port through microwave switches, followed by an isolator that mitigates detector back action [6], a band-pass filter centered at 6.0 GHz that limits the bandwidth for the heating signals to  $B_1 = 1500$  MHz [see Fig. 1(a)], and an infrared filter. Switching enables selection of five different drive lines, A–E, that are described later, in Sec. III, or a calibration reference source. We use a coaxial blackbody noise source from Ref. [47] mounted on the cold plate [Fig. 1(a), bottom left]; the impedance of the emitter is  $50 \Omega$  and its thermodynamic temperature  $T_{\text{bath}}$  as measured by a calibrated ruthenium oxide thermometer is varied between 0.12 and 1.5 K. Specifically, the calibration source emits quantum and classical noise, which is combined with a band-pass filter [Fig. 1(a)] to select a part of the blackbody spectrum around a center frequency of  $f = 5.8$  GHz and with a bandwidth of  $B_2 = 250$  MHz: the total noise power after the filter is approximately  $N_{\text{cal}} \approx \hbar\omega B_2 n_{\text{BE}}(T_{\text{bath}}, \omega)$ , where  $n_{\text{BE}}$  is given by Eq. (1). It is

important to note that drive lines A–E are used to inject active rf heating to the detector but, since they consist of cascaded attenuators, also emit a compound passive background noise power  $N_{\text{bb}} \approx \hbar\omega B_1 n_{\text{BE}}(T_{\text{bb}}, \omega)$ , where  $T_{\text{bb}}$  is the background temperature. In practice, we integrate  $n_{\text{BE}}$  over precharacterized transfer functions of the band-pass filters to account for the frequency dependence in Eq. (1) as well as any nonidealities in the transmission of the filters. The calibration relies on finding the  $T_{\text{bath}}$  that corresponds to a total power from a given input sources A–E. The dynamic range of the calibration is improved with the selection of overlapping bandwidths for which  $B_1 > B_2$ , which means that noise powers  $N_{\text{bb}}$  between 110 aW and 55 fW or, equivalently, temperatures  $T_{\text{bb}}$  between 72 and 400 mK, can be directly calibrated. Note that even in the limit of zero applied rf power, the temperature  $T_{\text{bb}}$  tends to a lower limit, labeled below as  $T_0$ , which will always be higher than the temperature of the base temperature stage of the refrigerator due to the cascaded nature of the system [see Sec. III A]. Conveniently, the strength of our methodology is that the total noise radiated into the sample space is precisely what we measure.

For the steady-state measurements, we define the response of the detector as a frequency sweep of the reflected microwave signal, which in practice we measure using a vector network analyzer (VNA, Keysight N5232B). In Figs. 1(b) and 1(c), we demonstrate the behavior of the bolometer resonance by plotting the real and imaginary parts of the reflected power around a probe frequency of 635 MHz. During heating with either a single-frequency rf drive (yellow) or the wide-band noise source (blue), the resonance frequency of the readout circuit is lowered with respect to no heating applied (gray), which is observable as a minute change in the reflected microwave probe signal. We quantify the equivalence of traces with a least-squares difference of the  $S$ -parameter traces as described in Appendix A. Note that the traces (yellow and blue) are nearly equal, which we observe as an overlap across all frequencies, i.e., the corresponding power from the drive line is calibrated. For equal responses, the following power balance holds at the calibration plane [see Fig. 1(a)]:

$$N_{\text{cal}} = \frac{P_{\text{gen}}}{L} + N_0, \quad (2)$$

where  $P_{\text{gen}}$  is the applied microwave power from a generator at room temperature (Rohde & Schwarz SGS100A), which is measured with a room-temperature power sensor (Keysight U2002A),  $N_0 = N_{\text{bb}}(T_0)$  is the background noise in the zero-power limit, and  $L = L(f_{\text{gen}})$  the line attenuation at the applied frequency  $f_{\text{gen}}$  in the filter pass band. As described below, the application is then to perform sweeps of noise-source temperature and generator power, allowing us to fit the unknown parameters  $N_0$

and  $L$  improving upon the single-point calibrations and even allowing noise calibration slightly below the dynamic range.

### 3. Measurement algorithm

We perform the power calibration method in two distinct ways. One way is to apply an rf power within the filter bandwidth around 6 GHz. Then, by taking a number of point-value pairs for equal responses ( $P_{\text{gen}}, N_{\text{cal}}$ ), we fit Eq. (2) as demonstrated in Fig. 1(d), where the error bars are combined statistical errors from the least-squares minimization of the calibration and the uncertainty of the room-temperature power sensor (for further details, see Appendix A). In this way, we obtain the attenuation  $L$  of the line and the intrinsic noise  $N_0$ , indicated by the nonzero offset in the inset and inverting the noise, we obtain the corresponding temperature  $T_0$ . Alternatively, we use a strong out-of-band tone at 800 MHz, which only serves to heat up the drive line and the last attenuator in particular. To evaluate the dissipated power, we modify the losses  $L$  measured around 6 GHz to account for the frequency dependence in conductor losses [50] present in the coaxial cables (more details are given in Appendix A). The heater tone itself is rejected by the band-pass filter (rejection at 0.8 GHz  $>80$  dB) and only noise emitted by the heated attenuator reaches the detector. In this case, if the noise powers are within the dynamic range of the noise source, the equivalent blackbody temperatures for the drive line are directly given by comparisons to the calibration set, yielding  $T_{\text{bb}} > T_0$ .

To translate the above to a recipe for steady-state measurements, we will consider the following practical measurement sequence. First, we toggle the microwave switches to the noise source and perform a temperature sweep to calibrate the detector. Before starting a measurement after a switching event, an idle time of 2 h is always adhered to. Second, for each of the drive lines A–E, we perform a power sweep at 5.8 GHz, an arbitrarily chosen frequency within the pass band, followed by a power sweep at another arbitrary in-band frequency of 6.0 GHz, and we only toggle to the next line after data for both frequencies have been collected. Third, another noise-source sweep is performed and added to the calibration set, also helping to verify that no significant drifting has occurred during sweeping. Finally, we cycle through each drive line again, performing high-power sweeps at 0.8 GHz using the previously obtained calibration set for this data.

### B. Dynamics

We turn to time-domain analysis of our drive lines under varying drive, which requires single-frequency readout of the detector. We now operate the VNA as a signal generator and inject power into the system at a single probe frequency while preserving the probe power level and

hence the operating point of the detector. In addition, we redirect the output signal from our detector to a lock-in amplifier instead of the VNA to better take advantage of the innately fast response time of the detector. In Fig. 2, we demonstrate usage of the detector in the time-resolving operating mode.

To calibrate measurements for a given drive line studied with single-frequency readout, we establish a link to the noise-source calibration of Sec. I by performing a reference measurement at 5.8 GHz. We apply a sequence depicted in Fig. 2(a): the applied generator power  $P_{\text{gen}}$  is kept at a steady level and then the power is stepped to a 3-dB lower value within a few nanoseconds, kept there for approximately 830 ms, and then near-instantaneously increased back to the steady-state level. Repeating this modulation pattern yields an ensemble-averaged signal that is rotated to a single quadrature and low-pass filtered, and a clear readout signal with a sharp response  $\Delta V$  is thus obtained. Light thresholding is also applied in post-processing to remove low-frequency interference with the readout signal, which we attribute to insufficient filtering below the inverse of the detector response time [43]. From a similar measurement with more averaging, we separately determine the response time of the detector and find it to be approximately 40  $\mu\text{s}$  for our chosen operating point, which sets the resolution of the dynamics that we may detect. The use of the difference in the digitizer voltage as the readout signal rather than the absolute signal level is designed to mitigate drifts that accumulate over long measurements. Repeating the sequence at many drive powers produces curves like the one shown in Fig. 2(b): the yellow points indicate the recorded responses against the change in rf power at the calibration plane ( $x$  axis) derived from the attenuation determined in Sec. I. We observe the linear dependence of the response against the power and perform a linear fit, in blue, giving us a method for calibrating small changes in unknown powers in subsequent measurements.

Now, the same pulse sequence is applied at a detuned frequency of 0.8 GHz, which exhibits a distinct heating response as shown in Fig. 2(c). We plot the data in blue and fit a single exponential, in yellow, separately to the rising and falling edges. Note the (4–5)-ms rise and decay time, which are approximately 2 orders of magnitude slower than the response time of the detector itself, which is strong direct evidence of attenuator heating. The dissipated power for the shown example trace is estimated to be approximately 0.5 nW. Such a measurement is repeated at many drive powers between hundreds of picowatts to tens of nanowatts. The single-time-constant approximation works well for small deviations in power as shown, while admitting that some evidence of a second much slower time constant is found at higher powers (not shown). For the purposes of this study, we only consider the faster time constant: the average of the rise and fall times is taken to be the representative time constant  $\tau$  for a drive power.

From the reference measurement of the corresponding drive line (line D as the example here), the obtained response  $\Delta V$  can be traced back to the noise-source calibration, yielding a corresponding change in noise power. We use such data to extend the temperature calibration below the dynamic range of the noise source, as we detail in Appendix A.

These measurements are, in practice, performed in the same cool-down, albeit separately, from the steady-state measurements, repeating a simple sequence for each of drive lines A–E: the reference and detuned measurements are performed in succession before moving the switch to the next position. The data obtained in this way are combined with steady-state data to obtain  $T_{\text{bb}}$  as a function of  $P_{\text{d}}$ . We use such data to calculate the thermal conductance  $G = dP_{\text{d}}/dT_{\text{bb}}$ . To take the derivative of noisy measurement data, we perform linear fits locally around each temperature point, including nine points for each fit, which effectively applies a moving-average operation to the data. The calculated thermal conductances and the fitted time constants are further used to estimate the thermal heat capacity, with  $C = \tau G$ .

### III. RESULTS

#### A. Drive-line configurations

We apply the detection mechanism and calibration schemes described in Sec. II to the problem of analyzing the noise power emitted from cryogenic wiring sets into the sample space. The interconnects are comprised of coaxial semirigid silver-plated cupronickel alloys with an outer cable diameter of 0.86 mm and SMA coaxial connectors [56]. Each cable spans two stages in the system, where the connection between two cables is made with a bulkhead connector, and on some stages the resistive microwave attenuators are installed. All attenuators placed inside the refrigerator include a nickel-chrome (Ni-Cr) thin-film resistor network as the attenuating element and may include other metals for heat-sinking purposes.

In addition, we always include 2 m of room-temperature coaxial cabling to interface with measurement electronics and short interconnects at 10 mK to reach the detector circuit of Fig. 1(a).

The drive-line configurations under study include typical attenuation schemes as described in Table I. Before entering the cryostat, lines A and E include room-temperature attenuation to maintain a comparable range of microwave powers at the quantum device without impacting the noise going into the system, which is well conditioned to 300 K. Inside the cryostat, the attenuation schemes are nominally identical between cryogenic stages at 300 and 1 K. However, for the two coldest stages of the system, at 0.1 and 0.01 K, we design an experiment with various microwave attenuators to detect resulting drive-line noise power variations with the calibrated detector. The three bottom rows of Table I summarize the experimental variations implemented, where the four different variables describe the attenuator construction, including (1) the casing material, (2) the interface style, (3) the substrate material, and (4) the attenuation value. The casing material has been selected to be either stainless steel (S) or C101 copper alloy (Cu). The interface style has been selected as either insertable (INS), with both a jack and a plug interface, or bulkhead (BH) with two jack interfaces. The substrate material is either amorphous alumina ( $\text{AlO}_x$ ) or crystalline sapphire (SAPH). The attenuation values for the experimental variations at the cold-plate and mixing-chamber (MXC) stages are chosen as either 20-dB or 30-dB reduction in power. Lines B–E share the same low-pass (LP) and infrared (IR) filtering at the coldest stage.

To set expectations for measurements, we note that lines A, B, and E in particular have gradual changes introduced between them and measurements should be directly comparable. Lines C and D may show much better noise characteristics, given their potentially superior material choices. We estimate the compound drive-line temperatures  $T_0$  that could theoretically be obtained in

TABLE I. A summary of the attenuator variations.

Cryo stage (K)	Line index				
	A	B	C	D	E
300	S-INS, 10 dB <sup>a</sup>	–	–	–	S-INS, 10 dB <sup>a</sup>
38	S-INS- $\text{AlO}_x$ , 1 dB				
3.0	S-INS- $\text{AlO}_x$ , 20 dB				
1.0	S-INS- $\text{AlO}_x$ , 0 dB				
	<i>experimental variations</i>				
0.1	S-INS- $\text{AlO}_x$ , 20 dB	S-INS- $\text{AlO}_x$ , 30 dB	Cu-BH- $\text{AlO}_x$ , 30 dB	Cu-INS-SAPH, 30 dB	S-INS- $\text{AlO}_x$ , 20 dB
0.01	S-INS- $\text{AlO}_x$ , 20 dB	S-INS- $\text{AlO}_x$ , 20 dB	Cu-BH- $\text{AlO}_x$ , 20 dB	Cu-BH-SAPH, 20 dB	S-INS- $\text{AlO}_x$ , 20 dB
	–	LP + IR filtering <sup>b</sup>			

<sup>a</sup>Room-temperature attenuator outside the refrigerator.

<sup>b</sup>Low-pass filter (Mini-Circuits ZLSS-8G-S+) and infrared filter (Bluefors).

the limit of no active rf power injected into the line in the unlikely scenario that the attenuators would fully thermalize to the stages on which they are mounted. In principle, cascaded attenuation thermalizes the line according to

$$n_i = \frac{n_{i-1}(\omega)}{L_i} + \frac{L_i - 1}{L_i} n_{\text{BE}}(T_i, \omega), \quad (3)$$

where for the  $i$ th stage, the  $L_i$  are the attenuation values in linear units,  $n_i$  is the photon number, and  $T_i$  is the temperature of the stage [2]. Based on the fixed attenuation values and the listed stage temperatures [Table I], using this model we estimate the theoretical lower limits for drive-line temperatures at 6 GHz to be 48 mK for lines A and E and 40 mK for B–D, respectively.

### B. Zero-power limit

We now perform a  $Y$ -factor measurement (see Sec. II A 2) of the drive lines, applying a heater tone between 0.1 and 1.8 fW at the calibration plane. In Fig. 3, we show results of two characterizations at 5.8 GHz (yellow) and 6.0 GHz (blue), both frequencies within the detector bandwidth. Figures 3(a) and 3(b) correspond to the attenuation  $L$  and residual background noise  $N_0$  of Eq. (2), respectively.

The attenuation in Fig. 3(a) is approximately 80 dB for all lines, which is consistent with 61 or 71 dB of fixed attenuation in the dilution refrigerator, 10 or 0 dB at room temperature, and an expected contribution from cable losses. We observe a maximal difference of 1 dB

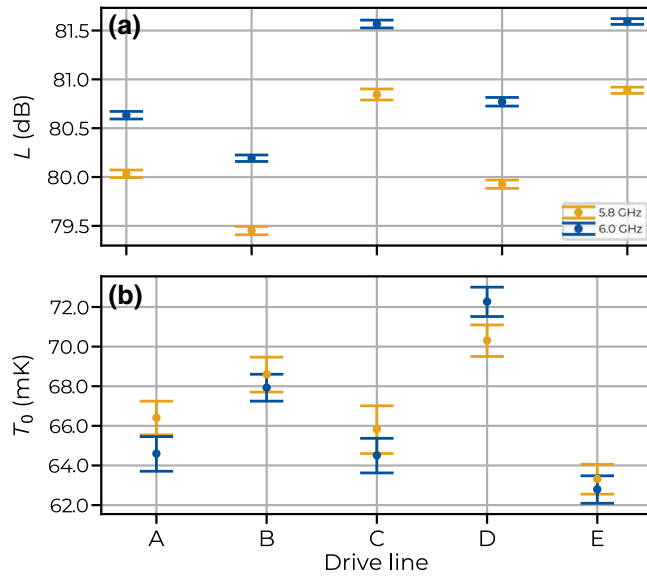


FIG. 3. Results from the  $Y$ -factor analysis of drive lines A–E at 5.8 and 6.0 GHz: in both panels, the error bars correspond to two-standard-deviation fitting error. (a) The line attenuation. (b) The residual background thermal-noise temperature.

in attenuation between lines B and E: the specifications for the attenuators allow variation up to  $\pm 0.5$  dB for the 20-dB insertable variant and  $\pm 0.75$  dB for any other kind with 20 dB or more attenuation. Some variation may also be attributed to difference in cable lengths in particular, since we are including 2 m of room-temperature cabling in each line. For the lossy coaxial lines used between temperature stages (8 dB/m at 300 K and 6 GHz), we estimate that a difference of at least 12 cm would be needed to sum up to 1 dB. In reality, the difference in cable lengths is at most a few centimeters. On the other hand, the difference between the results at 5.8 and 6.0 GHz is consistently 0.6–0.8 dB, which gives further confidence in our method. The observed increase in losses from 5.8 GHz to 6.0 GHz consists of frequency-dependent effects, including 0.2 dB from increased conductor loss, 0.1 dB from low-pass filtering in the case of B–E, and a measured 0.4 dB from variation in reflection from the detector. We argue that while there is always loss due to the imperfect match to  $50 \Omega$ , amounting to approximately 0.5 dB as estimated in Ref. [45], its effect on systematic error in  $T_0$  will be minimized and calibrated out due to (1) the integrating nature of the detector (2) the presence of similar average loss independent of which filter path is chosen. The frequency-dependent cable losses and calibration errors due to the detector mismatch are discussed in more detail in Appendix A 2.

Taking the average of the blue and yellow points for a given drive line in Fig. 3(b), the noise temperatures vary between 63 and 71 mK, corresponding to a 70% increase in thermal photons at 6 GHz. We see a maximum of 2 mK of variation between any pair of results, which can be explained by means of measurement uncertainty. Crucially, the integrated noise should not and does not change when the applied rf frequency changes, since the noise bandwidth is kept the same, which highlights the robustness of the calibration method. The lowest temperature is obtained with insertable stainless steel attenuators that are low-pass filtered (line E), although the difference to lines A and C is barely beyond the measurement uncertainty. Furthermore, at these low noise temperatures we do not see a statistically significant benefit (line A versus line E) from filtering, which is reasonable considering that the filter cut-off at 7.5 GHz is much above our measurement bandwidth. A more noticeable difference of only a few millikelvin can be seen to the hotter line B and the hottest line D, where the latter includes low-pass-filtered attenuators with a sapphire substrate. In theory, sapphire should provide the coldest environment, typically assuming a thermal conductivity at least an order of magnitude higher [57] than that of alumina, which suggests that something else is limiting thermalization.

Based on these data alone, it is difficult to recommend a particular material or filtering choice. As we will see in Sec. III C, more insight can be gained by applying

higher powers or utilizing the time-resolving mode. In fact, based on these results, none of the lines seem particularly well thermalized, in contrast to Eq. (3): we see photon numbers between 5 and 20 times as high as the predicted numbers. In particular, for lines B–D we note that the 30-dB attenuators at the cold plate do not bring any benefit given the low powers, where dissipation should not be an issue. We also acknowledge that the goal has not been to reach the coldest possible temperatures but to test a common drive-line configuration. Improvements are clearly possible with a different distribution of the attenuation [30] or more filtering [13]. Additionally, note that here we have assumed an idealized blackbody spectrum as per Eq. (1) and we have focused only on a narrow band of that spectrum, whereas, in reality, filtering the drive line should make the spectrum nonthermal. In the context of qubit readout, further damping occurs in the less-than-unity coupling to the readout resonator, which is also verified using an open quantum system approach later,

in Sec. IV. Overall, the results that we obtain are in agreement with dephasing rates and corresponding temperatures reported in the literature [11–13,17,20,58].

### C. High-power thermodynamics

We now explore the physical limits of the drive lines by dissipating nanowatts of rf power in the rejection band of the detection circuit at 0.8 GHz, which leads to measurable noise emission within the measurement bandwidth around 6 GHz. As described in Sec. II, the measurements include steady-state drive with VNA readout and square-pulse modulated drive to create small 3-dB deviations around a steady power, requiring readout with a lock-in amplifier. The dissipated powers  $P_d$  in the last 20-dB attenuator of each drive line are estimated from the attenuation factors determined in Sec. II, taking the frequency-dependent cable losses into account (see details in Appendix A). The high-power steady-state measurements remain within the

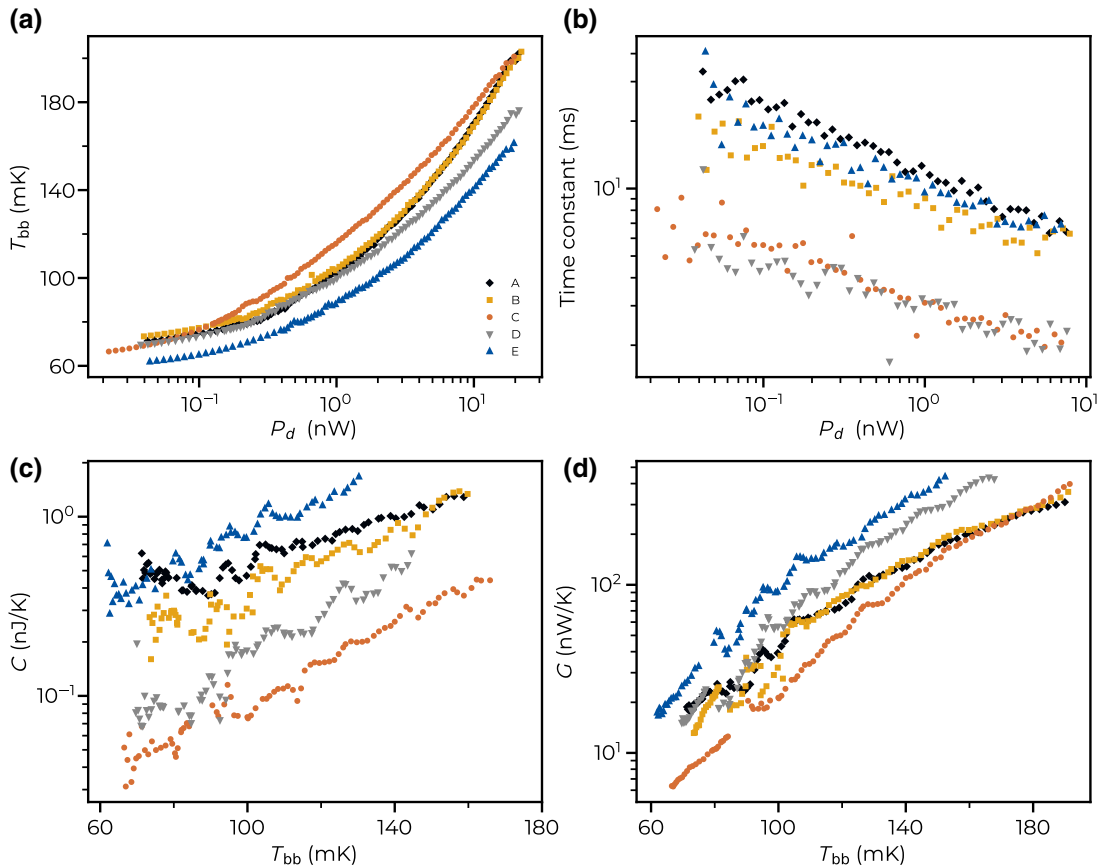


FIG. 4. Drive lines A–E during high-power rf drive at a detuned frequency of 0.8 GHz. (a) The equivalent blackbody temperature versus the power dissipated in the last attenuator. (b) The time constant for 3-dB power excursions from steady state. (c) The thermal heat capacity. (d) The thermal conductance. In (a), (c), and (d), the data for A–E are a combination of high-power steady-state measurements with direct calibration using the noise-source and low-power pulsed measurements with extended calibration below  $\{0.2, 0.2, 0.2, 0.2, 0.4\}$  nW, respectively (for details, see Sec. II). The fitting error in the noise temperatures is of the order of marker size, in time constants 10% on average, and for most thermal conductance points below 20%, leading to below 30% error in thermal capacity. From attenuator specifications, the powers in lines A, B, and E have additional systematic uncertainty of  $\pm 0.5$  dB, and  $\pm 0.75$  dB for lines C and D.

TABLE II. Selected drive-line parameters for lines A–E evaluated at  $T_{\text{bb}} = 100$  mK and power laws fitted at  $T_{\text{bb}} > 100$  mK.

Line index	$C$ (pJ/K)	$G$ (nW/K)	$\tau$ (ms)	$C \propto T^x$	$G \propto T^x$
A	480	40	12	1.7	3.0
B	290	27	11	2.5	3.2
C	76	21	3.6	3.5	4.4
D	180	56	3.2	3.1	4.0
E	770	92	8.4	2.0	3.3

dynamic range of the noise source and therefore allow direct calibration of the blackbody temperature  $T_{\text{bb}}$  and below approximately 80 mK we extend this calibration to the time-domain data. The most important application of the time-domain measurement is to reveal the thermal time constants, capacity, and conductance. The combined measurement results are shown in Fig. 4 and key metrics are displayed in Table II.

In Fig. 4(a), we display the equivalent blackbody temperatures of the drive lines as a function of the power dissipated in the last 20-dB attenuator. We see that all attenuators are limited to temperatures between 62 and 73 mK at the lowest powers applied, which are in accordance with the  $Y$ -factor analysis of Sec. II. The corresponding noise powers are within  $-8\%$  to  $+40\%$  of those displayed in Sec. II, indicating that lines A and B, in particular, have not been measured at low enough powers to completely remove the effect of active heating. At higher powers, the differences between the lines become more apparent, with the temperatures ranging from 160 mK to 200 mK at 20 nW. The coldest line at all powers is line E, as has also been found before.

As another important metric, we observe the time constants as a function of the dissipated power in Fig. 4(b). Across all powers, it is immediately obvious that there is almost an order-of-magnitude decrease in time constants comparing the insertable attenuator geometries to bulk-heads, assuming that the last attenuator is the defining factor. For instance, the fastest to thermalize are lines C and D, which reach approximately 2 ms at 1 nW, and the slowest is line A, reaching 12 ms at the same power.

We may now calculate the heat capacities, shown in Fig. 4(c). The results range from tens of pJ/K to a few nJ/K at the lowest temperatures obtained, which implies significant variations in thin-film volumes. Our first observation is that the lines containing BH-type attenuators, lines C and D, have the lowest heat capacities across all measured temperatures, up to an order of magnitude smaller than the INS attenuators, which indicates smaller thin-film volumes inside the more compact casing. Despite some scatter in the data, we fit power laws of the form  $C \propto T^x$  to the data above 100 mK and obtain exponents between 1.7 and 3.5. Although only indicative, all the numbers are above 1, which directly violates the free-electron model of

$C_e = \gamma T$  that would be the expected behavior in metals at low temperatures [57]. The detector senses electron temperatures via photonic radiation and therefore we do not expect to sense phonon terms of  $\propto T^3$  in the heat capacity. Remarkably, the lowest number corresponds to the unfiltered line A, suggesting that absorption is taking place in the filters in case of the other lines that share the same physical filter components. We have not detected any of this with the  $Y$ -factor analysis and it only becomes evident at higher powers. We also note that the superlinear behavior could be attributed to errors in the estimation of the dissipated power or, more likely, noise emitted by the cold-plate attenuators, for which we do not presently correct.

Finally, in Fig. 4(d), we show the thermal conductance as a function of the temperature. We observe a strong temperature dependence across all drive lines A–E. Expressed by a power law above 100 mK, the powers vary between 3.0 and 4.4, which is a narrower spectrum in contrast to that seen on the heat capacities. As expected, the values are mostly in agreement with the clean electron-phonon coupling of  $G \propto T^4$  [31], confirming that it is the dominant mechanism for heat conduction at high temperatures. At low temperatures, the power laws are not well defined due to discontinuities in the data.

To summarize the above, all of the attenuators reach similar levels of noise in the low-power limit but the effective dynamic range is where the largest differences are seen. Better power handling has been demonstrated elsewhere by adding large volumes of copper heat sinks on top of the resistor thin films [58]. The use of sapphire as a substrate instead of alumina should bring additional benefits, even though we did not find strong evidence here, in particular, due to the perceived large variance in thin-film volumes. In future measurements, control experiments with more comparable volumes should be performed. In addition, to improve the accuracy of the measured heat capacity of the attenuator at the MXC stage, the following procedure could be implemented. First, remove the attenuator at the MXC stage and repeat the power detection measurements. Second, compare the  $T_{\text{bb}}$  of the system before and after removal of the attenuator to determine the thermodynamic temperature of the removed attenuator. Finally, use the thermodynamic temperature of the attenuator at the MXC stage as the input to the heat capacity calculation above.

#### IV. DISCUSSION

In the following, we present theoretical estimations on how the blackbody temperatures of Fig. 4(a) would influence the dynamics of a transmon qubit under realistic operational conditions. In principle, to fully account for the dynamics of the line, one should consider the thermal transients induced in the line during a microwave control

pulse [see the rising side of Fig. 2(c)] characterized by a thermal latency time constant  $\tau$ , with the power dependence captured in Fig. 4(b). However, we are able to simplify the analysis to a steady-state scenario based on a quick calculation as we now describe. Assume that the drive line is at its base temperature  $T_0$  [Fig. 3(a)] and, for qubit operations, a rather long 1- $\mu$ s square pulse is applied at a voltage level corresponding to  $P_d = 20$  nW: the maximal power during measurements and in the calculations below. Across all drive lines A–E, we take the highest measured temperature from Fig. 4(a) and at that temperature we extrapolate the lowest time constant from Fig. 4(b), both of which occur for line C, making it the worst-case example. At the maximal steady-state temperature of 200 mK, we find  $\tau \approx 1.5$  ms, yielding only a negligible increase of 0.09 mK during the qubit pulse. From now on, we do not need to model the temperature rise during individual pulses but, rather, we apply individual pulses, starting from a steady-state temperature that has resulted from an average power drive [see Fig. 4(a)] prior to the pulse that we study. We consider two specific line configurations, labeled C and E, corresponding to the cases in which the lines heat up the most and the least, respectively. This section is divided into two subsections, the first of which includes a model of the qubit-drive-line system, while the second includes projections on the impact of drive-line heating on coherence and gate fidelities.

### A. Model

The circuit that we consider consists of a fixed-frequency transmon qubit that is coupled capacitively to a readout resonator and a direct  $X$ - $Y$  line. The interaction between the qubit and the resonator is dispersive and modeled by the Jaynes-Cummings Hamiltonian [5]. Moreover, the resonator is capacitively coupled to its own drive line. The impact of the noise injected by the  $X$ - $Y$  line can be quantified using an open quantum system approach that models the drive line as a bosonic bath coupled to the  $\sigma_y$  Pauli operator. Under these assumptions, the  $X$ - $Y$  line induces relaxation and decoherence described by the following relaxation time [7]:

$$T_{1,xy} = \frac{C_\Sigma(\omega_q^2 + \omega_{co}^2)}{ZC_{xy}^2\omega_q^2\omega_{co}^2 \coth\left(\frac{\hbar\omega_q}{2k_B T_{xy}}\right)}. \quad (4)$$

In Eq. (4),  $\omega_{co}$  is a cutoff frequency,  $\omega_q$  is the qubit transition frequency,  $\omega_r$  is the resonator frequency,  $Z$  is the impedance of the drive line,  $C_{xy}$  is the  $X$ - $Y$  line coupling capacitance to the qubit,  $C_q$  is the qubit capacitance,  $C_\Sigma = C_{xy} + C_q$  is the total capacitance to ground, and  $T_{xy} = T_{bb}$  is the drive-line temperature with the link to  $P_d$ , the power dissipated in the last attenuator, given by Fig. 4(a). As for the type of noise coming from the resonator drive line, this

is also assumed to be thermal and it induces pure dephasing [5] on the qubit, quantified by a pure dephasing time  $T_\phi$ . The values that we use for all our calculations are  $Z = 50 \Omega$ ,  $\omega_q = 2\pi \times 6.043$  GHz,  $C_q = 0.468$  pF,  $\omega_r = 2\pi \times 4.781$  GHz,  $\chi = 2\pi \times 9.59$  MHz,  $\kappa = 2\pi \times 88$  kHz,  $T_{1,int} = 300 \mu$ s,  $\omega_{co} = 2\pi \times$  THz,  $g = 2\pi \times 110$  MHz, and, unless mentioned otherwise,  $C_{xy} = 117$  aF. Here, we include an internal relaxation time  $T_{1,int}$ , motivated by recent experiments [14–16], with the total  $T_1$  then determined by the two rates, i.e.,  $T_1^{-1} = T_{1,xy}^{-1} + T_{1,int}^{-1}$ . In principle, the calculations in Sec. IV B could also be performed using higher  $T_{1,int}$  with the same Lindblad-based approach, provided that the Born-Markov approximation is still valid. At the power levels measured in Fig. 4(a), the ratio  $T_{1,xy}/T_{1,int}$  would range between 0.3 and 0.5. Additionally,  $\kappa$  is the resonator line width and  $\chi$  is the dispersive shift, needed to estimate the dephasing time  $T_\phi$  [18,59], giving the decoherence time  $T_2^* = 1/[(2T_1)^{-1} + T_\phi^{-1}]$ .

Since we are considering a direct  $X$ - $Y$  line, the pulse duration needed to fully excite the qubit with a  $\pi$  pulse [2,4] reads

$$\tau_p = 3\sqrt{\frac{2\hbar\pi(L_{MXC} - 1)}{P_d} \frac{C_\Sigma}{C_{xy}}}, \quad (5)$$

where  $L_{MXC} = 100$  is the last-stage attenuation connecting the dissipated power to the drive power at the sample input. Applying Eq. (5), we obtain a realistic [60,61] pulse duration of 22 ns at the maximal power of  $P_d = 20$  nW. The coupling value  $C_{xy}$  above has been selected because it maximizes  $T_2^*/\tau_p$  when the resonator drive line is cooled down to 20 mK. Additional details on qubit control and coupling optimization are given in Appendix B.

### B. Coherence and fidelity calculations

We investigate the power dependence of the qubit time constants when driving separately either through the  $X$ - $Y$  line or the resonator drive line. The results are displayed in Fig. 5. In Figs. 5(a) and 5(b), we show the dependence of  $T_1$  and  $T_2^*$  on the power dissipated in the  $X$ - $Y$  drive line, using the parameters listed in Sec. IV A. We stress that no power is sent through the resonator drive line, the temperature of which is set to its baseline value of 65 mK, resulting in a constant  $T_\phi$  over the whole range of dissipated powers. We observe a decreasing trend  $T_1$  with increasing dissipated power. Line E shows saturation to about 182  $\mu$ s below 0.1 nW, which is attributed to the limit set by  $T_{1,int}$ . The decoherence  $T_2^*$  shows a very weak dependence on the dissipated power and it is instead mostly dominated by the constant pure dephasing rate resulting from the 65-mK noise injected by the resonator line. By increasing  $T_{1,int}$ , higher saturation values for both  $T_1$  and  $T_2^*$  will be observed. However, longitudinal

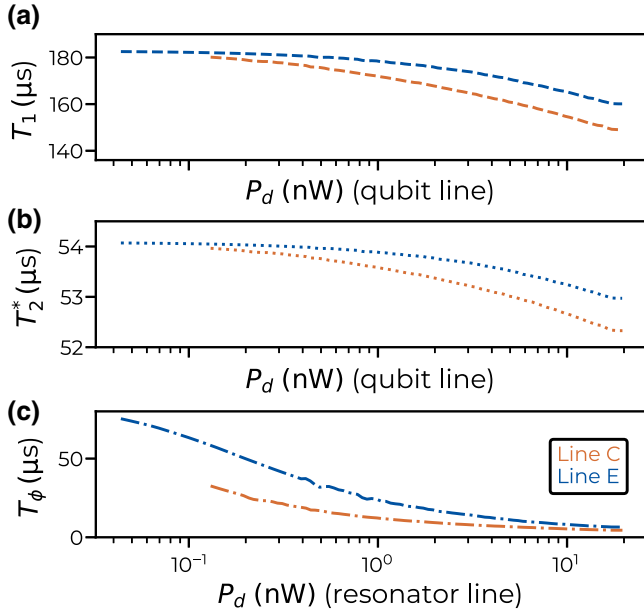


FIG. 5. (a) The longitudinal relaxation time  $T_1$  for drive-line configurations C and E, as functions of the dissipated power at optimal drive-line coupling to the qubit. The temperature of the resonator drive line is assumed stationary and is set at 65 mK. (b) The transverse relaxation time  $T_2^*$  for lines C and E, calculated using the same parameters as in (a). (c) The dephasing time  $T_\phi$  as a function of the power dissipated in the resonator line for lines C and E.

relaxation will become increasingly dominated by the  $X$ - $Y$  control noise, making the effect more apparent. In contrast, in Fig. 5(c), the dephasing time  $T_\phi$  is a lot more sensitive to stronger power levels that in this case are dissipated in the resonator drive line. We observe an order-of-magnitude drop in the dephasing time from the lowest applied powers to the highest at 20 nW. The investigated range of powers can be compared to the critical photon number  $n_{\text{crit}} = |\omega_r - \omega_q|^2 / (4g^2)$  [4], which sets the upper bound for the validity of the dispersive approximation. In practice, the photon number  $n_{\text{crit}}$  also acts as a rough guide for the optimal readout power, although recent studies [62,63] have shown that it does not necessarily set a strict upper limit. For our chosen parameters, the critical photon number translates to a  $P_d$  below 3 fW [64], which is low enough to suggest headroom to increase the coupling  $\kappa$  by a few orders of magnitude without heating up the line. For the remainder of this section, we shift our focus to qubit control operations. To estimate directly the ability to perform gate operations using the control lines described above, we consider the average gate-fidelity formula derived in Ref. [65] for Lindblad master equations. In the model that we consider here, this fidelity reads

$$F_N = 1 - \frac{dN\tau}{2(d+1)} \left( \frac{1}{T_1} + \frac{1}{T_\phi} \right), \quad (6)$$

where  $\tau$  is a gate duration,  $N$  is the number of qubits involved, and  $d = 2^N$ . The above equation has been derived for a local noise model acting linearly on each qubit independently and thus does not account for qubit-qubit crosstalk noise. Nonetheless, it can provide a lower bound on single- and two-qubit gate operations performed at the power levels considered here. We first consider single-qubit rotations ( $N = 1$ ) and, consistently with our previous findings, we assume a typical pulse duration  $\tau = 22$  ns, which corresponds to an optimized setup in which  $C_{xy} \approx 117$  aF, at  $P_{\text{diss}} = 20$  nW (see Appendix B). Using Eq. (6), we estimate the average fidelity of 99.97% for line C and 99.98% for line E. In contrast, considering the same operations at a much stronger coupling of  $C_{xy} = 4.6$  fF, requiring a low power of  $P_d = 0.1$  nW, would lead to stronger decoherence and lower average fidelities dipping all the way down to 96.6%.

We extend the above to a circuit with two transmon qubits. Each one is coupled to their own separate  $X$ - $Y$  control lines and readout resonators. Moreover, the resonators are coupled to their own control lines, which introduce dephasing on the relevant qubit. Finally, we couple the two qubits dispersively using a circuit element, e.g., a resonator. We consider the cross-resonance (CR) gate [66,67] which, being an all-microwave two-qubit gate, is applicable to this type of circuit. The gate is implemented by driving the control qubit at the resonance frequency of the target qubit. Because of the qubit-qubit coupling, Rabi oscillations will be induced on the target qubit with a period that depends on the state of the control qubit. Using the simplified model in Ref. [4], we can estimate a typical CR pulse duration using the circuit outlined above. If we assume a typical qubit-qubit detuning  $\Delta = 0.3$  GHz, a qubit-qubit coupling  $J = 0.01$  GHz  $\ll \Delta$ ,  $C_{xy} = 117$  aF, and  $P_{\text{diss}} = 20$  nW, we obtain a CR duration  $\tau_{\text{CR}} \approx 450$  ns, consistent with values recorded in the literature [4]. This time, we set  $N = 2$  in Eq. (6) resulting in a modified prefactor of 4/5. As mentioned above, we neglect qubit-qubit crosstalk, and therefore obtain an upper bound to the actual fidelity value. Using the above parameters, we estimate these bounds at 98.64% and 99.29% for lines C and E, respectively.

In our analysis above, we observe that the elevated line temperatures do not appear to impact gate fidelities of operations as much as the  $X$ - $Y$  coupling strength, which instead leads to a more dramatic performance deterioration. However, we note that dephasing noise stemming from the resonator line is the main limiting factor. Thus, efforts should be directed at improving thermalization and signal conditioning in this line specifically. All in all, the calculations here prove that both lines are suitable for typical single- and two-qubit gate operations, as long as the  $X$ - $Y$  coupling capacitance is not too large. Ideally, one should have  $10^{-4} \leq C_{xy}/C_\Sigma \leq 10^{-3}$  (for further details on coupling optimization, see Appendix B).

## V. CONCLUSIONS

In conclusion, our measurements of drive-line temperatures explain typical dephasing rates from the literature that are higher than predicted from a simple cascaded attenuator model. At a high microwave power, the standard insertable attenuators have achieved lower temperatures than bulkhead geometries at equivalent power, which has been supplemented with direct evidence of the thermal latencies and derived heat capacities of the former surpassing those of the latter by almost an order of magnitude. The results underline the importance of maximizing thin-film volumes and introducing heat sinks in resistive attenuators for improving their power handling. We have performed a theoretical analysis of a realistic qubit-resonator system and drawn the following conclusions: (1) at typical power levels, the single- and two-qubit gate durations are such that thermal latencies are not a primary concern and (2) for qubits with a state-of-art quality factor, the average fidelities can be reasonably high if an optimized trade-off between power levels and qubit-line coupling is implemented. Our experimental results have been achieved with a new cryogenic rf power-calibration method using a coaxially coupled temperature-variable blackbody radiation source in conjunction with an *in situ* power detector maintaining traceability to primary standards. The nanobolometer that we have chosen as the detector has the advantage of a high dynamic range and a wide bandwidth, and can be used in a time-resolving mode. Overall, our methodology enables direct studies in noise dynamics of amplifier back action or emerging technologies including flexible wiring, photonic links, or cryo-CMOS electronics.

## ACKNOWLEDGMENTS

We acknowledge useful discussions with Nurul Huda, Leif Roschier, and David Gunnarsson from Bluefors, and Mikko Möttönen from Aalto University. Additionally, we thank Joel Hunnako (Bluefors) for supplementary cable-loss data.

The authors of this paper have a financial interest in the field of cryogenic engineering. All authors are employed by Bluefors Oy in Helsinki, Finland.

## APPENDIX A: CALIBRATION DETAILS

### 1. Procedure

The steady-state measurements rely on generating a calibration set. As explained in Sec. II A, we sweep  $T_{\text{bath}}$  and map out the detector response. For a power  $P_{\text{gen}}$ , as measured by a room-temperature power sensor, applied to the drive line, we find the equivalent response from the calibration set by following a very similar logic to “Method 1” of Ref. [45] but instead of a known dc power dissipated on chip, we have a known rf noise power. In essence, we

compute residuals of the form

$$\sum_{f_p} \{ \text{Re}[\Delta S_{21}(f_p)] \}^2 + \{ \text{Im}[\Delta S_{21}(f_p)] \}^2, \quad (\text{A1})$$

where  $f_p$  is a probe frequency point and  $\Delta S_{21} = S_{21}^{\text{gen}} - S_{21}^{\text{cal}}$ , with the  $S$  parameters referring to the responses of the applied power and those of the calibration set, respectively. A parabola is fitted around the minimum of the function, yielding a calibrated noise power  $N_{\text{cal}}$ . Using the statistical uncertainties of the polynomial coefficients, the two-standard-deviation statistical error, labeled as  $E_N$ , in the calibrated noise power is calculated. The uncertainty in power  $P_{\text{gen}}$  is  $E_P = 0.04 \times P_{\text{gen}}$  according to the data sheet of the room-temperature sensor [68].

In the steady-state measurements around 6 GHz, repeating the calibration procedure above for a number of  $P_{\text{gen}}$  allows fitting point-value pairs  $(P_{\text{gen}}, N_{\text{cal}})$  to Eq. (2) using a weighted linear fit with weights  $1/\sqrt{E_P^2 + E_N^2}$ . This results in the attenuation  $L$  and background noise power  $N_0$  and two-standard-deviation errors for both quantities, as seen in Fig. 3. The obtained losses include fixed attenuation as well as coaxial cable loss that depends primarily on the frequency-dependent conductor losses [50]. For the data of Fig. 4, the dissipated power  $P_d$  in the last stage has therefore been evaluated using

$$P_d = \frac{P_{\text{gen}} L_{\text{MXC}}}{L(f_{\text{gen}})} \left[ \frac{L(0)}{L(f_{\text{gen}})} \right]^{\left( \frac{f_{\text{stop}}}{f_{\text{gen}}} \right)^{\frac{1}{2}} - 1}, \quad (\text{A2})$$

where  $L_{\text{MXC}}$  is the attenuation value at the last stage,  $f_{\text{stop}} = 800$  MHz is the detuned drive frequency, and  $L(0)$  is the known fixed attenuation. In particular, data measured at  $f_{\text{gen}} = 5.8$  GHz are used to perform the cable-loss correction. On the other hand, calibrating the noise powers at the detuned frequency is more complicated: when above the dynamic range of the noise source ( $> 80$  mK), noise powers are directly calibrated with the steady-state measurements and the corresponding temperatures  $T_{\text{bb}}$  are also above 80 mK. This constitutes the majority of the data points in Fig. 4(a). The high-power nature of these measurements makes the noise  $N_{\text{bb}}$  a function of power and thus renders Eq. (2) useless. The calibration below the dynamic range needs to be performed in a different way. In practice, we make use of the sensitive single-frequency readout in the time-resolving mode and extend the calibration there.

In the time-resolving mode, we perform readout at a single probe frequency, as we have described in Sec. II B. A separate noise-source calibration is not performed here, since we do not have a compatible normalization technique to eliminate drift in the weak digitizer signals. We extend the calibration from above to these measurements using the

determined attenuation to precisely determine the power in the reference measurement at 5.8 GHz.

The power sweeps performed during the reference measurement yield calibration sets for time-domain signals as shown in Fig. 2(b). The same pulse sequence is repeated out of band at 800 MHz, giving the time-domain responses  $\Delta V$  of the drive line and the time constants for the cooling and heating times  $\tau_{\text{cooling}}$  and  $\tau_{\text{heating}}$  with their average  $\tau = (\tau_{\text{cooling}} + \tau_{\text{heating}})/2$ , plotted in Fig. 4(b). We estimate the error in  $\tau$  from the difference  $E_\tau = (\tau_{\text{cooling}} - \tau_{\text{heating}})/2$ . The responses are calibrated against the reference, giving corresponding changes in powers  $\Delta N_{\text{pulsed}}$ . The result of the detuned measurements is a set of point-value triplets  $(\tau, \Delta P_d, \Delta N_{\text{pulsed}})$  that are used below.

For the noise  $N_{\text{pulsed}}$  at a dissipated power  $P_d$ , the following holds:

$$N_{\text{pulsed}}(P_d) = \int_\epsilon^{P_d} \frac{dN_{\text{pulsed}}}{dP_d} dP_d + N_\epsilon. \quad (\text{A3})$$

We may then interpolate  $dN_{\text{pulsed}}/dP_d$  over dissipated powers  $P_d$  and integrate, giving us the total emitted noise at a power  $P = P_d$  minus a constant  $N_\epsilon$  that should reach  $N_0$  at  $P_d \rightarrow 0$ . As an estimate for  $N_\epsilon$ , we take the average difference of the first ten points of noise-source-calibrated  $N_{\text{cal}}$  and interpolated  $N_{\text{pulsed}}$ . In this way, we extend our calibration below the range  $N_{\text{pulsed}}(P_d)$  versus  $P_d$  collected with the direct noise-source calibration of Sec. II A 2. We prefer to use the direct calibration when powers are in the dynamic range of the noise source due to the relatively large steps in power that are used to estimate the derivative even though, in principle, single-frequency readout allows better sensitivity.

## 2. Systematic errors in calibrated losses and powers

The systematic and random error sources in the above calibration are discussed in Secs. III B and III C. We demonstrate two key systematic error sources in Fig. 6. For the losses  $L$  around the microwave frequency of 6 GHz in particular [Fig. 3(a)], a dominant systematic error source can be ascribed to the variations in the reflection magnitude of the detection circuit. To characterize this error, we perform a supplementary measurement in another cool-down and display the results in Fig. 6(a). In the yellow trace, a detector steady-state calibration (see above) is performed at a fixed generator power and the generator frequency  $f_{\text{gen}}$  is varied from 5 to 7 GHz. From the obtained power-absorption data  $N_{\text{cal}}(f_{\text{gen}})$ , the transmission is calculated from Eq. (2) ignoring the negligible offset. For reference, the data in the blue trace correspond to the band-pass filter “1” [see Sec. II] measured with a VNA at room temperature. In both cases, the obtained transmission magnitudes  $1/L$ , or, equivalently,  $|S_{21}|$ , are normalized with cable losses and fixed attenuation around the center of the pass band: a linear fit to the transmission data in decibels

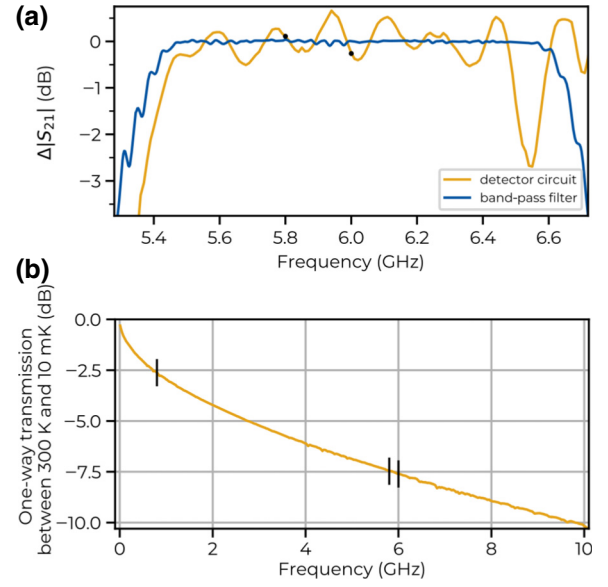


FIG. 6. Two sources of systematic error in loss and power calibration. (a) Systematic error in calibration of losses due to impedance mismatch in the detector circuit. The yellow line shows the loss-normalized transmission of the drive line, as observed with the detector at 10 mK. The black points indicate uncorrected systematic error for data in Fig. 3(a). The blue line shows the normalized transmission of the detector band-pass filter at room temperature, measured with a VNA. (b) The yellow line shows the one-way transmission averaged from measurements of 24 lines with S-Cu-Ni coaxial lines spanning cryogenic stages between 300 K and 10 mK. The measurements have been performed at base temperature, utilizing loop-back connections at the 10-mK stage. The black vertical lines indicate the microwave frequencies 0.8 GHz, 5.8 GHz, and 6.0 GHz chosen for measurements in the main text, with respective loss values of 2.62 dB, 7.47 dB, and 7.61 dB.

versus the square root of the frequency. In particular, the black points in the figure correspond to data of Fig. 3 and their difference of 0.4 dB explains a large part of the difference between the fitted loss values  $L$ , and in principle the error could be corrected. We expect that for broadband sources, such as the thermal noise that we measure in the main text, this error should be smaller due to the integration across the filter bandwidths that the detector performs.

The drive-line losses that determine the dissipated powers around the detuned frequency of 800 MHz [Fig. 4] cannot be directly measured in our measurement setup within a single cool-down. Although the fixed attenuation does not have innate frequency dependence, the cable losses have a dependence as shown in Fig. 6(b) and in agreement with Eq. (A2). The one-way losses are estimated from looped-back line measurement statistics collected from cool-downs in the same dilution refrigerator that we have used for the experiments here. The lines have

been unattenuated but otherwise nominally of the same type (S-Cu-Ni, 0.86 mm) as those considered in the main text, except that room-temperature cabling has not been included. In our experiment here, the one-way losses of the lines can be directly measured although only inside the detector bandwidth, and therefore we rely on Eq. (A2) to correct for the frequency dependence of the cable losses at out-of-band frequencies, as part of the power calibration described in Sec. A 1. Using detector-measured loss values at 5.8 GHz to perform the loss conversion to the 800-MHz cable-loss equivalent, we note that the loss values in decibels are reduced by a factor of 3. Together with the small mismatch error at 5.8 GHz [Fig. 6(a)], which could in principle also be corrected, and having performed the loss correction, the dissipated power values of Fig. 4 have remaining uncharacterized error as per the attenuator specifications (either 0.5 dB or 0.75 dB for the nominally 20 dB INS- and BH-type attenuators, respectively).

## APPENDIX B: QUBIT CONTROL

We estimate the required pulse duration  $\tau_p$  for a given fixed coupling. Here, we consider a Gaussian pulse modulated by a sinusoidal driving at the resonant frequency of the qubit  $\omega_q$ , implementing a standard  $\pi$  pulse. The voltage wave traveling to the qubit down the drive line reads

$$V(t) = \Omega_0 e^{-\frac{t^2}{2\sigma^2}} \sin(\omega_q t + \phi_0), \quad (\text{B1})$$

where  $\Omega_0$  is the Rabi frequency,  $\sigma$  is the pulse full width at half maximum, and  $\phi_0$  is the initial voltage phase. The Rabi frequency  $\Omega_0$  is directly connected to the dissipated power at the qubit via the following relation [4]:

$$\Omega_0 = \frac{C_{xy}}{C_\Sigma} \sqrt{\frac{P_d}{(L_{\text{MXC}} - 1)\hbar}}, \quad (\text{B2})$$

where  $L_{\text{MXC}} = 100$  accounts for dissipation at the last attenuation stage. Thus, the dissipated powers are converted to the actual powers delivered to the qubit. The practical pulses that we consider are truncated to a pulse duration of [2]:

$$\tau_p \equiv 6\sigma = 6 \sqrt{\frac{\pi}{2\Omega_0^2}}. \quad (\text{B3})$$

We will now connect the pulse durations to the coupling capacitance  $C_{xy}$ . Using Eq. (4) along with the results of Fig. 4(a), we plot the qubit dynamical parameters in Fig. 7 as a function of the qubit-drive-line coupling for two different values of the resonator drive-line temperatures, set at 20 mK and 65 mK and shown in Figs. 7(a) and 7(b), respectively. In this example, the qubit is driven at the maximum dissipated power measured in our experiment,

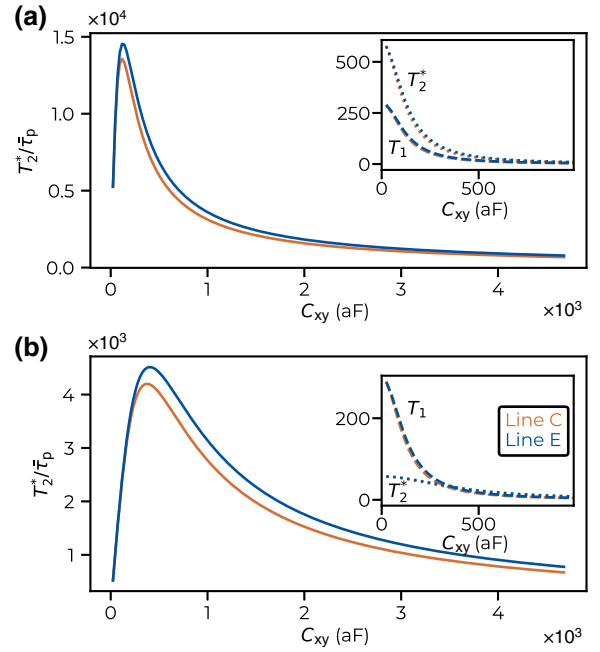


FIG. 7. The ratios between  $T_2^*$  and the average pulse duration  $\bar{\tau}_p$  plotted as a function of the capacitance coupling  $C_{xy}$  for drive-line configurations C and E, with resonator drive-line temperatures set at (a) 20 mK and (b) 65 mK, respectively. For both lines, the power dissipated in the last attenuator is 20 nW. In the inset, using the same parameters, the longitudinal and transverse relaxation times,  $T_1$  and  $T_2^*$ , are shown over a wider range of coupling values.

about 20 nW, leading to the strongest heat-up. In the main panels, we show the ratio of  $T_2^*$  to  $\bar{\tau}_p$ , demonstrating similar behavior at both resonator line temperatures. Two observations can be made. First, even at maximum dissipated power (i.e., maximum  $T_{xy}$ ), the average single-qubit pulse duration is several order of magnitudes shorter than the transverse relaxation time, as one should expect. Second, we observe an optimal value for the qubit-drive-line coupling that maximizes  $T_2^*$  relative to  $\bar{\tau}_p$ . The calculated peak values for  $T_2^*/\tau_p$  for both lines depend strongly on the temperature of the resonator line, which ranges from about 4000 to 13 000. Similarly, the peak coupling values  $C_{xy}$  roughly triple when going from 20 to 65 mK, switching from 117 to 374 aF. In both panels, the insets show how the longitudinal and transverse relaxation times decay as functions of  $C_{xy}$ . Even though both  $T_1$  and  $T_2^*$  are slightly larger for line E than for line C, as one would expect, they vanish very quickly as the qubit-drive-line coupling is increased.

The optimal coupling values observed in Fig. 7 originate from two competing effects. On the one hand, the line-qubit coupling should be strong enough to allow for state manipulation. On the other hand, however, it should introduce the least thermal noise possible on the qubit. In fact, the peak value can be calculated analytically, leading

to the following equation:

$$C_{xy}^* = \sqrt{\frac{C_q(\omega_q^2 + \omega_{co}^2)}{Z\omega_q^2\omega_{co}^2 \coth\left(\frac{\hbar\omega_q}{2k_B T_{xy}}\right)} \frac{2T_{1,int} + T_\phi}{T_\phi T_{1,int}}}, \quad (\text{B4})$$

which connects directly the optimal qubit-drive-line coupling to the resonator temperature via the dephasing time  $T_\phi = \Gamma_\phi^{-1}$  calculated from standard models [18,59]. We argue that one should not design the coupling to the qubit based on the resonator line temperature, which may be improved with further signal conditioning, whereas the drive-line heating will always be present to some degree if high powers and duty cycles are used. For this reason, we choose the peak position from Fig. 7(a), evaluated at  $C_{xy}^* \approx 117$  aF, for our calculations in the main text. We acknowledge that the same applies to the selection of an arbitrary  $T_{1,int}$ , although we have included the limit in the optimization of the coupling here.

- [1] F. Arute, *et al.*, Quantum supremacy using a programmable superconducting processor, *Nature* **574**, 505 (2019).
- [2] S. Krinner, S. Storz, P. Kurpiers, P. Magnard, J. Heinsoo, R. Keller, J. Lütolf, C. Eichler, and A. Wallraff, Engineering cryogenic setups for 100-qubit scale superconducting circuit systems, *EPJ Quantum Technol.* **6**, 1 (2019).
- [3] A. Blais, A. L. Grimsmo, S. M. Girvin, and A. Wallraff, Circuit quantum electrodynamics, *Rev. Mod. Phys.* **93**, 025005 (2021).
- [4] P. Krantz, M. Kjaergaard, F. Yan, T. P. Orlando, S. Gustavsson, and W. D. Oliver, A quantum engineer's guide to superconducting qubits, *Appl. Phys. Rev.* **6**, 021318 (2019).
- [5] A. Vaaranta, M. Cattaneo, and R. E. Lake, Dynamics of a dispersively coupled transmon qubit in the presence of a noise source embedded in the control line, *Phys. Rev. A* **106**, 042605 (2022).
- [6] A. A. Clerk, M. H. Devoret, S. M. Girvin, F. Marquardt, and R. J. Schoelkopf, Introduction to quantum noise, measurement, and amplification, *Rev. Mod. Phys.* **82**, 1155 (2010).
- [7] M. Cattaneo and G. S. Paroanu, Engineering dissipation with resistive elements in circuit quantum electrodynamics, *Adv. Quantum Technol.* **4**, 2100054 (2021).
- [8] Y. Lu, N. Lambert, A. F. Kockum, K. Funo, A. Bengtsson, S. Gasparinetti, F. Nori, and P. Delsing, Steady-state heat transport and work with a single artificial atom coupled to a waveguide: Emission without external driving, *PRX Quantum* **3**, 020305 (2022).
- [9] A. P. Sears, A. Petrenko, G. Catelani, L. Sun, H. Paik, G. Kirchmair, L. Frunzio, L. I. Glazman, S. M. Girvin, and R. J. Schoelkopf, Photon shot noise dephasing in the strong-dispersive limit of circuit QED, *Phys. Rev. B* **86**, 180504(R) (2012).
- [10] D. Ristè, C. C. Bultink, M. J. Tiggelman, R. N. Schouten, K. W. Lehnert, and L. DiCarlo, Millisecond charge-parity fluctuations and induced decoherence in a superconducting transmon qubit, *Nat. Commun.* **4**, 1913 (2013).
- [11] F. Yan, S. Gustavsson, A. Kamal, J. Birenbaum, A. P. Sears, D. Hover, T. J. Gudmundsen, D. Rosenberg, G. Samach, S. Weber, J. L. Yoder, T. P. Orlando, J. Clarke, A. J. Kerman, and W. D. Oliver, The flux qubit revisited to enhance coherence and reproducibility, *Nat. Commun.* **7**, 12964 (2016).
- [12] F. Yan, D. Campbell, P. Krantz, M. Kjaergaard, D. Kim, J. L. Yoder, D. Hover, A. Sears, A. J. Kerman, T. P. Orlando, S. Gustavsson, and W. D. Oliver, Distinguishing coherent and thermal photon noise in a circuit quantum electrodynamical system, *Phys. Rev. Lett.* **120**, 260504 (2018).
- [13] A. Somoroff, Q. Ficheux, R. A. Mencia, H. Xiong, R. Kuzmin, and V. E. Manucharyan, Millisecond coherence in a superconducting qubit, *Phys. Rev. Lett.* **130**, 267001 (2023).
- [14] A. P. M. Place, *et al.*, New material platform for superconducting transmon qubits with coherence times exceeding 0.3 milliseconds, *Nat. Commun.* **12**, 1779 (2021).
- [15] J. Biznárová, A. Osman, E. Rehnman, L. Chayanun, C. Križan, P. Malmberg, M. Rommel, C. Warren, P. Delsing, A. Yurgens, J. Bylander, and A. F. Roudsari, Mitigation of interfacial dielectric loss in aluminum-on-silicon superconducting qubits, *ArXiv:2310.06797*.
- [16] M. Bal, *et al.*, Systematic improvements in transmon qubit coherence enabled by niobium surface encapsulation, *npj Quantum Inf.* **10**, 43 (2024).
- [17] J.-H. Yeh, J. LeFebvre, S. Premaratne, F. C. Wellstood, and B. S. Palmer, Microwave attenuators for use with quantum devices below 100 mK, *J. Appl. Phys.* **121**, 224501 (2017).
- [18] Z. Wang, S. Shankar, Z. K. Mineev, P. Campagne-Ibarcq, A. Narla, and M. H. Devoret, Cavity attenuators for superconducting qubits, *Phys. Rev. Appl.* **11**, 014031 (2019).
- [19] I. M. Pop, K. Geerlings, G. Catelani, R. J. Schoelkopf, L. I. Glazman, and M. H. Devoret, Coherent suppression of electromagnetic dissipation due to superconducting quasiparticles, *Nature* **508**, 369 (2014).
- [20] M. Reagor, W. Pfaff, C. Axline, R. W. Heeres, N. Ofek, K. Sliwa, E. Holland, C. Wang, J. Blumoff, K. Chou, M. J. Hatridge, L. Frunzio, M. H. Devoret, L. Jiang, and R. J. Schoelkopf, Quantum memory with millisecond coherence in circuit QED, *Phys. Rev. B* **94**, 014506 (2016).
- [21] C. Wang, Y. Y. Gao, P. Reinhold, R. W. Heeres, N. Ofek, K. Chou, C. Axline, M. Reagor, J. Blumoff, K. M. Sliwa, L. Frunzio, S. M. Girvin, L. Jiang, M. Mirrahimi, M. H. Devoret, and R. J. Schoelkopf, A Schrödinger cat living in two boxes, *Science* **352**, 1087 (2016).
- [22] D. I. Schuster, A. Wallraff, A. Blais, L. Frunzio, R.-S. Huang, J. Majer, S. M. Girvin, and R. J. Schoelkopf, ac Stark shift and dephasing of a superconducting qubit strongly coupled to a cavity field, *Phys. Rev. Lett.* **94**, 123602 (2005).
- [23] P. Bertet, I. Chiorescu, G. Burkard, K. Semba, C. J. P. M. Harmans, D. P. DiVincenzo, and J. E. Mooij, Dephasing of a superconducting qubit induced by photon noise, *Phys. Rev. Lett.* **95**, 257002 (2005).
- [24] P. Bertet, I. Chiorescu, C. J. P. M. Harmans, and J. E. Mooij, Dephasing of a flux-qubit coupled to a harmonic oscillator, *ArXiv:cond-mat/0507290*.
- [25] L. S. Bishop, J. M. Chow, J. Koch, A. A. Houck, M. H. Devoret, E. Thuneberg, S. M. Girvin, and R. J. Schoelkopf,

- Nonlinear response of the vacuum Rabi resonance, *Nat. Phys.* **5**, 105 (2009).
- [26] C. Rigetti, J. M. Gambetta, S. Poletto, B. L. T. Plourde, J. M. Chow, A. D. Córcoles, J. A. Smolin, S. T. Merkel, J. R. Rozen, G. A. Keefe, M. B. Rothwell, M. B. Ketchen, and M. Steffen, Superconducting qubit in a waveguide cavity with a coherence time approaching 0.1 ms, *Phys. Rev. B* **86**, 100506(R) (2012).
- [27] B. Suri, Z. K. Keane, R. Ruskov, L. S. Bishop, C. Tahan, S. Novikov, J. E. Robinson, F. C. Wellstood, and B. S. Palmer, Observation of Autler-Townes effect in a dispersively dressed Jaynes-Cummings system, *New J. Phys.* **15**, 125007 (2013).
- [28] X. Y. Jin, A. Kamal, A. P. Sears, T. Gudmundsen, D. Hover, J. Miloshi, R. Slattery, F. Yan, J. Yoder, T. P. Orlando, S. Gustavsson, and W. D. Oliver, Thermal and residual excited-state population in a 3D transmon qubit, *Phys. Rev. Lett.* **114**, 240501 (2015).
- [29] J. Goetz, S. Pogorzalek, F. Deppe, K. G. Fedorov, P. Eder, M. Fischer, F. Wulschner, E. Xie, A. Marx, and R. Gross, Photon statistics of propagating thermal microwaves, *Phys. Rev. Lett.* **118**, 103602 (2017).
- [30] M. Scigliuzzo, A. Bengtsson, J.-C. Besse, A. Wallraff, P. Delsing, and S. Gasparinetti, Primary thermometry of propagating microwaves in the quantum regime, *Phys. Rev. X* **10**, 041054 (2020).
- [31] F. C. Wellstood, C. Urbina, and J. Clarke, Hot-electron effects in metals, *Phys. Rev. B* **49**, 5942 (1994).
- [32] A. G. Fowler, M. Mariantoni, J. M. Martinis, and A. N. Cleland, Surface codes: Towards practical large-scale quantum computation, *Phys. Rev. A* **86**, 032324 (2012).
- [33] D. J. Reilly, Engineering the quantum-classical interface of solid-state qubits, *npj Quantum Inf.* **1**, 15011 (2015).
- [34] A. D. Córcoles, A. Kandala, A. Javadi-Abhari, D. T. McClure, A. W. Cross, K. Temme, P. D. Nation, M. Steffen, and J. M. Gambetta, Challenges and opportunities of near-term quantum computing systems, *Proc. IEEE* **108**, 1338 (2020).
- [35] J. P. Smith, B. A. Mazin, A. B. Walter, M. Daal, J. Bailey, C. Bockstiegel, N. Zobrist, N. Swimmer, S. Steiger, and N. Fruitwala, Flexible coaxial ribbon cable for high-density superconducting microwave device arrays, *IEEE Trans. Appl. Supercond.* **31**, 1 (2021).
- [36] D. Underwood, *et al.*, Using cryogenic CMOS control electronics to enable a two-qubit cross-resonance gate, *PRX Quantum* **5**, 010326 (2024).
- [37] F. Lecocq, F. Quinlan, K. Cicak, J. Aumentado, S. A. Diddams, and J. D. Teufel, Control and readout of a superconducting qubit using a photonic link, *Nature* **591**, 575 (2021).
- [38] K. Usami and Y. Nakamura, A photonic link for quantum circuits, *Nat. Electron.* **4**, 323 (2021).
- [39] S. Gasparinetti, K. L. Viisanen, O.-P. Saira, T. Faivre, M. Arzeo, M. Meschke, and J. P. Pekola, Fast electron thermometry for ultrasensitive calorimetric detection, *Phys. Rev. Appl.* **3**, 014007 (2015).
- [40] M. Partanen, K. Y. Tan, J. Govenius, R. E. Lake, M. K. Mäkelä, T. Tanttu, and M. Möttönen, Quantum-limited heat conduction over macroscopic distances, *Nat. Phys.* **12**, 460 (2016).
- [41] B. Karimi, F. Brange, P. Samuelsson, and J. P. Pekola, Reaching the ultimate energy resolution of a quantum detector, *Nat. Commun.* **11**, 367 (2020).
- [42] K. Inomata, Z. Lin, K. Koshino, W. D. Oliver, J.-S. Tsai, T. Yamamoto, and Y. Nakamura, Single microwave-photon detector using an artificial  $\Lambda$ -type three-level system, *Nat. Commun.* **7**, 12303 (2016).
- [43] J. Govenius, R. E. Lake, K. Y. Tan, and M. Möttönen, Detection of zeptojoule microwave pulses using electrothermal feedback in proximity-induced Josephson junctions, *Phys. Rev. Lett.* **117**, 030802 (2016).
- [44] R. Kokkonieni, J. Govenius, V. Vesterinen, R. E. Lake, A. M. Gunyhó, K. Y. Tan, S. Simbierowicz, L. Grönberg, J. Lehtinen, M. Prunnila, J. Hassel, A. Lamminen, O.-P. Saira, and M. Möttönen, Nanobolometer with ultralow noise equivalent power, *Commun. Phys.* **2**, 124 (2019).
- [45] J.-P. Girard, R. E. Lake, W. Liu, R. Kokkonieni, E. Visakoppi, J. Govenius, and M. Möttönen, Cryogenic sensor enabling broad-band and traceable power measurements, *Rev. Sci. Instrum.* **94**, 054710 (2023).
- [46] A. M. Gunyhó, S. Kundu, J. Ma, W. Liu, S. Niemelä, G. Catto, V. Vadimov, V. Vesterinen, P. Singh, Q. Chen, and M. Möttönen, Single-shot readout of a superconducting qubit using a thermal detector, *Nat. Electron.* **7**, 288 (2024).
- [47] S. Simbierowicz, V. Vesterinen, J. Milem, A. Lintunen, M. Oksanen, L. Roschier, L. Grönberg, J. Hassel, D. Gunnarsson, and R. E. Lake, Characterizing cryogenic amplifiers with a matched temperature-variable noise source, *Rev. Sci. Instrum.* **92**, 034708 (2021).
- [48] J. Engert, D. Heyer, and J. Fischer, Low-temperature thermometry below 1 K at PTB, *AIP Conf. Proc.* **1552**, 136 (2013).
- [49] J. Engert, A. Kirste, A. Shibahara, A. Casey, L. V. Levitin, J. Saunders, O. Hahtela, A. Kemppinen, E. Mykkänen, M. Prunnila, D. Gunnarsson, L. Roschier, M. Meschke, and J. Pekola, New evaluation of  $T - T_{2000}$  from 0.02 K to 1 K by independent thermodynamic methods, *Int. J. Thermophys.* **37**, 125 (2016).
- [50] D. Pozar, *Microwave Engineering* (Wiley, Hoboken, NJ, 2012), 4th ed.
- [51] K. Serniak, M. Hays, G. de Lange, S. Diamond, S. Shankar, L. D. Burkhardt, L. Frunzio, M. Houzet, and M. H. Devoret, Hot nonequilibrium quasiparticles in transmon qubits, *Phys. Rev. Lett.* **121**, 157701 (2018).
- [52] K. Serniak, S. Diamond, M. Hays, V. Fatemi, S. Shankar, L. Frunzio, R. Schoelkopf, and M. Devoret, Direct dispersive monitoring of charge parity in offset-charge-sensitive transmons, *Phys. Rev. Appl.* **12**, 014052 (2019).
- [53] A. P. Vepsäläinen, A. H. Karamlou, J. L. Orrell, A. S. Dogra, B. Loer, F. Vasconcelos, D. K. Kim, A. J. Melville, B. M. Niedzielski, J. L. Yoder, S. Gustavsson, J. A. Formaggio, B. A. VanDevender, and W. D. Oliver, Impact of ionizing radiation on superconducting qubit coherence, *Nature* **584**, 551 (2020).
- [54] A. D. Córcoles, J. M. Chow, J. M. Gambetta, C. Rigetti, J. R. Rozen, G. A. Keefe, M. Beth Rothwell, M. B. Ketchen, and M. Steffen, Protecting superconducting qubits from radiation, *Appl. Phys. Lett.* **99**, 181906 (2011).
- [55] V. Tripathi, H. Chen, E. Levenson-Falk, and D. A. Lidar, Modeling low- and high-frequency noise in transmon

- qubits with resource-efficient measurement, *PRX Quantum* **5**, 010320 (2024).
- [56] Bluefors, Coaxial Wiring, <https://bluefors.com/products/measurement-infrastructure/coaxial-wiring/>.
- [57] F. Pobell, *Matter and Methods at Low Temperatures* (Springer-Verlag, Berlin, 2007), 3rd ed.
- [58] J.-H. Yeh, Y. Huang, R. Zhang, S. Premaratne, J. LeFebvre, F. C. Wellstood, and B. S. Palmer, Hot electron heatsinks for microwave attenuators below 100 mK, *Appl. Phys. Lett.* **114**, 152602 (2019).
- [59] A. A. Clerk and D. W. Utami, Using a qubit to measure photon-number statistics of a driven thermal oscillator, *Phys. Rev. A* **75**, 042302 (2007).
- [60] F. Motzoi, J. M. Gambetta, P. Rebentrost, and F. K. Wilhelm, Simple pulses for elimination of leakage in weakly nonlinear qubits, *Phys. Rev. Lett.* **103**, 110501 (2009).
- [61] R. Barends, *et al.*, Superconducting quantum circuits at the surface code threshold for fault tolerance, *Nature* **508**, 500 (2014).
- [62] Y. Sunada, S. Kono, J. Ilves, S. Tamate, T. Sugiyama, Y. Tabuchi, and Y. Nakamura, Fast readout and reset of a superconducting qubit coupled to a resonator with an intrinsic Purcell filter, *Phys. Rev. Appl.* **17**, 044016 (2022).
- [63] M. F. Dumas, B. Groleau-Paré, A. McDonald, M. H. Muñoz-Arias, C. Lledó, B. D’Anjou, and A. Blais, Unified picture of measurement-induced ionization in the transmon, *ArXiv:2402.06615*.
- [64] A. Bruno, G. de Lange, S. Asaad, K. L. van der Enden, N. K. Langford, and L. DiCarlo, Reducing intrinsic loss in superconducting resonators by surface treatment and deep etching of silicon substrates, *Appl. Phys. Lett.* **106**, 182601 (2015).
- [65] T. Abad, J. Fernández-Pendás, A. Frisk Kockum, and G. Johansson, Universal fidelity reduction of quantum operations from weak dissipation, *Phys. Rev. Lett.* **129**, 150504 (2022).
- [66] C. Rigetti and M. H. Devoret, Fully microwave-tunable universal gates in superconducting qubits with linear couplings and fixed transition frequencies, *Phys. Rev. B* **81**, 134507 (2010).
- [67] J. M. Chow, A. D. Córcoles, J. M. Gambetta, C. Rigetti, B. R. Johnson, J. A. Smolin, J. R. Rozen, G. A. Keefe, M. B. Rothwell, M. B. Ketchen, and M. Steffen, Simple all-microwave entangling gate for fixed-frequency superconducting qubits, *Phys. Rev. Lett.* **107**, 080502 (2011).
- [68] Keysight, U2000 Series USB Power Sensors—Keysight, <https://www.keysight.com/zz/en/assets/7018-01515/datasheets/5989-6278.pdf>.